

# Landslides Triggered by Recent Earthquakes in Italy



Ernesto Ausilio, Francesco Silvestri, Giuseppe Tropeano,  
and Paolo Zimmaro

**Abstract** This document provides a detailed description of seismically-induced landslides and rockfalls that occurred in Italy during the 2016 Central Italy earthquake sequence. Relevant ground motion characteristics for all mainshocks of the sequence are analyzed. The document also provides a quantitative overview of spatial and temporal characteristics of the landslides and rockfalls that occurred during the earthquake sequence which was characterized by three mainshocks: (1) **M**6.1 on 24 August, (2) **M**5.9 on 26 October, and (3) **M**6.5 on 30 October. A relevant fraction of landslides has been caused by the first **M**6.1 mainshock; however, both the following events, especially the third **M**6.5 earthquake, exacerbated the slope instability in many locations and triggered several new and more serious ground failures. The overwhelming majority of the instabilities induced by the sequence are rockfalls in fractured rocks. Details of three selected case histories are described: (1) the Nera rockslide, (2) the Pescara del Tronto landslide, and (3) the Accumoli landslide. Rainfall data during 2016 are also shown and described for selected locations in the epicentral area.

---

E. Ausilio · P. Zimmaro (✉)  
University of Calabria, Rende, Italy  
e-mail: [pzimmaro@ucla.edu](mailto:pzimmaro@ucla.edu)

E. Ausilio  
e-mail: [ernesto.ausilio@unical.it](mailto:ernesto.ausilio@unical.it)

F. Silvestri  
University of Napoli Federico II, Napoli, Italy  
e-mail: [francesco.silvestri@unina.it](mailto:francesco.silvestri@unina.it)

G. Tropeano  
University of Cagliari, Cagliari, Italy  
e-mail: [giuseppe.tropeano@unica.it](mailto:giuseppe.tropeano@unica.it)

P. Zimmaro  
University of California, Los Angeles, USA

## 1 Introduction

Landslides have been considered as secondary effects induced by earthquakes. These local phenomena affect the areas of interest and can substantially aggravate the seismic impact on human, social, and economic resilience during the aftermath. Recently, several studies have focused on the roles played by these secondary effects in the extents of damage and loss of human life (e.g., Bird and Bommer 2004).

Italy is characterized by very frequent seismic activity and high geomorphological and hydrological hazards. As a result, in recent years, numerous earthquakes were recorded in Italy, causing ground failures including landslides and rockfalls. Before 1783, historical accounts of the occurrence of earthquake-induced landslides were typically incomplete and vague (Keefer 2002). The first scientific post-earthquake reconnaissance including systematic documentation of landslides induced by earthquakes was undertaken in the Calabria region (Southern Italy) following the 1783 Calabrian earthquake sequence (Sarconi 1784, quoted by Cotecchia et al. 1986).

In the last century, Ambraseys (1976) and Govi (1977) documented ground failures triggered by the 1976 Friuli (Northern Italy) earthquake sequence, in which landslides were almost entirely rockfalls. Instability phenomena associated with the 1980 Irpinia earthquake (Southern Italy) were characterized by delayed initiation or reactivation. Cotecchia and Del Prete (1984) and D'Elia et al. (1985) observed coherent slides and earth flows that began moving between a few hours to a few days after the mainshock. These phenomena were associated with increased spring flow and pore-water pressures. This has resulted in an anomalous distribution of landslides where landslides were more numerous at greater distances from the epicenter. More recently, ground failures triggered by the 1997 Umbria-Marche (Central Italy) earthquake were mainly disrupted landslides. The areal distribution of landslides in Umbria-Marche was characterized by a large number of slope instabilities in the area adjacent to the epicentral area, with a decreasing trend with distance (Bozzano et al. 1998; Esposito et al. 2000).

In the period between August 24, 2016, and January 20, 2017, a wide area in Central Italy underwent a seismic sequence with three major earthquakes. The first event that had a moment magnitude  $M = 6.1$  occurred on August 24, 2016, the second ( $M = 5.9$ ) on October 26, and the third ( $M = 6.5$ ) on October 30, 2016. Each event was followed by numerous aftershocks.

The Mt. Vettore-Mt. Bove normal fault system caused all mainshocks of the sequence. The first mainshock (occurred on August 24, 2016) caused extensive damage especially to the villages of Amatrice, Accumoli, and Arquata del Tronto. The earthquake sequence caused 299 fatalities, generally from total collapses of unreinforced masonry buildings. The two mainshocks occurred in October caused massive new damage in the villages of Visso, Ussita, and Norcia. After the 24 August event, the epicentral area of the October earthquakes had largely been evacuated. As a result, these additional events did not produce fatalities.

Several landslides and rockfalls were triggered by the seismic sequence (Ausilio et al. 2019). The volume and area of the landslides caused by the August mainshock

were limited despite that the regional morphology was steep and that a significant seasonal rainfall had occurred in the week preceding the August earthquake. For the instabilities triggered by the August event, this document focuses on the results (and subsequent analysis) of reconnaissance missions performed by the following agencies:

- (1) The Geotechnical Extreme Event Reconnaissance Association (GEER 2016, 2017),
- (2) The National Institute for Environmental Protection and Research (ISPRA 2016),
- (3) The Research Center for Prediction, Prevention and Monitoring of Geological Risks of Sapienza University (CERI 2016),
- (4) The National Institute for Geophysics and Volcanology (INGV 2016).

Information about landslide features triggered and/or exacerbated by the October events are mainly based on observations made by the GEER team and CERI. The authors of this document participated in the GEER reconnaissance mission and subsequent analysis. The GEER reconnaissance mission was conducted during two phases:

- (1) Following the 24 August event, from early September to early October 2016,
- (2) Following the October events, between the end of November and the beginning of December 2016.

For the 26 October event, limited field observations are described from the short time window between this event and the subsequent 30 October event and do not include detailed mapping. As a result, more emphasis is placed on features triggered by the 24 August event, and exacerbated and/or triggered by the October events (i.e., observed during the second reconnaissance trip following the 30 October event).

The large majority of the observed instability features are rockfalls in fractured rocks. Many rockfalls observed after the October events are likely due to breakage of joints that were likely weakened by the 24 August event. The document describes the following three major landslides that were judged as valuable case histories:

- The slope failure on the south-western flank of the Nera River valley, south-west of the village of Visso, where a large rockslide took place at the time of the M6.5 earthquake on 30 October 2016;
- Pescara del Tronto, where the 2016 events induced significant instabilities in a soil/rock slopes overlooking the SS4 motorway which connects the west to the east coast of Central Italy and hence is a very important transportation infrastructure;
- Accumoli, where the southern spur of a hill failed in spite of a village located atop.

For the Accumoli and Pescara del Tronto landslide case histories, particular attention was paid to the incremental damage (or lack thereof) caused by multiple events. This idea was particularly relevant as these areas were inspected repeatedly after both the 24 August and 26–30 October earthquakes. These multiple technical visits made it possible to document the damage level following each earthquake. This area

of Central Italy has been affected by a large number of historical coseismic rockfalls. For example, previous studies by Antonini et al. (2002), Carro et al. (2003), and Gigli et al. (2014) documented and analyzed rockfall hazard and risk in the Umbria-Marche Apennine area of Central Italy following the 1997–1998 Umbria-Marche earthquake.

## 2 Seismic Sources and Ground Motion

The Central Apennine chain can be seen as the backbone of the Italian peninsula. The whole region is characterized by extensional tectonic activity. This regional extension is accommodated, in the inner Central Apennines, by a series of normal faults striking northwest-southeast (NW–SE) and dipping south-west (SW). Seismological, geometric, and kinematic characteristics of the main seismogenic sources of the area are summarized in GEER (2016, 2017) and Galadini et al. (2018).

This is a region with a long history of destructive earthquakes. The locations of faults have been well studied, and the effects of past earthquakes on villages and towns in the region is well documented. The 2016 earthquake sequence in Central Italy occurred in a seismic gap between two earlier earthquakes, which are the 1997 **M6.1** Umbria-Marche earthquake to the northwest and the 2009 **M6.1** L'Aquila earthquake to the southeast (Fig. 1a). Figure 1b shows the main active fault segments in the epicentral area of the 2016 Central Italy earthquake sequence. The **M6.1** event on 24 August was a peculiar two-fault event caused by the rupture in the southernmost section of the Mt. Vettore-Mt. Bove fault system (MVBF in Fig. 1b) in association with the rupture of the northernmost section of the Laga Mts. fault system (Amatrice segment, AF in Fig. 1b). On the other hand, both the 26 and 30 October events occurred solely on the Mt. Vettore-Mt. Bove fault system. Table 1 shows parameters and locations of the mainshocks and three main aftershocks (after Galadini et al. 2018).

### 2.1 August 24, 2016 Event

The mainshock occurred on the August 24, 2016, at 01:36:32 (UTC) and was recorded by Italian National Seismic Networks (Rete Sismica Nazionale, RSN; [www.gm.ingv.it/index.php/retesismica-nazionale/](http://www.gm.ingv.it/index.php/retesismica-nazionale/), last accessed November 21, 2016) owned by the Italian Institute of Geophysics and Volcanology (Istituto Nazionale di Geofisica e Vulcanologia, INGV). The August 24, 2016, mainshock event occurred along segments of normal fault systems trending NW–SE (strike ~165 degrees) with a dip angle SW of ~45 degrees. The strike of the fault from the moment tensor is generally consistent with the orientation of the Mt. Vettore fault to the north and the Laga Mountain fault to the south. As mentioned earlier, the event occurred as a result of



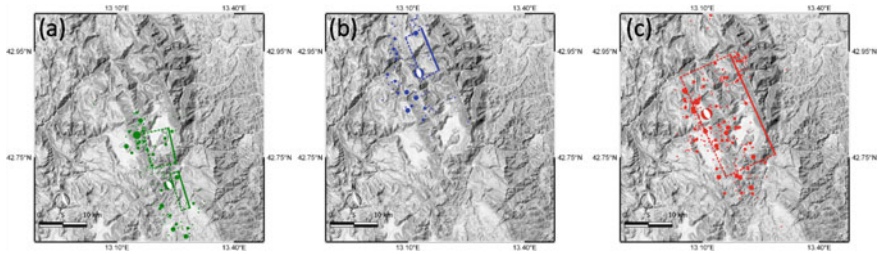


**Fig. 2** Trimmed finite fault model, moment tensor, and epicenter location for the **a** M6.1 on 24 August, **b** M5.9 on 26 October, and **c** 30 October event, along with aftershocks recorded within 24-h periods following each mainshock

a multi-fault rupture between two-fault systems, the Mt. Vettore-Mt. Bove and the Laga.

Figure 2a shows the surface projection of the trimmed finite fault model for this event. The two-fault systems involved in this rupture are: the Laga Mountains fault system (Amatrice segment) and the Mt. Vettore-Mt. Bove fault system. The number of aftershocks within the 24-h periods following the 24 August mainshock was 121. Most of the aftershock epicenters are not within the surface projection of the hanging wall above the finite fault model, with many south and west of the rupture (Fig. 2a).

## 2.2 October 26 and 30, 2016 Events

The location of hypocenters, slip directions and surface rupture suggest that the events on 26 and 30 October were accompanied by ruptures in the segments of the Mt. Vettore-Mt. Bove Fault. As described in GEER (2016), this fault and the neighboring Laga Mts. fault to the south experienced rupture during the 24 August event.

The 26 October event has an along-strike length of 8 km and down-dip width of 4 km. The 30 October event has an along-strike length of 21 km and down-dip width of 16 km. Figures 2b, c shows the epicenter location and surface fault projection for the 26 and 30 October events, respectively, along with aftershocks recorded within 24 h of each mainshock.

Figure 3 shows the cumulative fault offset measurement (70 cm) on the lower or “western” fault trace (Lat = 42.812901°, Long = 13.24626°). A comprehensive overview of the fault surface rupture observed during the 2016 Central Italy earthquake sequence is provided by GEER (2017) and Gori et al. (2018).

The number of aftershocks within the 24-h period following each mainshock was 75 (26 October), and 258 (30 October). Aftershocks following these mainshocks have clear spatial patterns (Fig. 2b, c). For the 26 October event, very few aftershocks actually occur within the surface projection of the rupture. The aftershocks pattern





**Fig. 3** Incremental surface fault rupture on the western slope of Mt. Vettore-Mt. Bove fault

for the largest event (30 October) suggests, as expected, that most epicenters are situated within the surface projection of the rupture.

Figure 4 shows the spatial distribution of peak ground acceleration (PGA) in the epicentral area for all three mainshocks. Also shown in Fig. 4 is the location of selected case histories. The measures of the ground motion intensity presented in this figure were estimated using kriging of within-event residuals (i.e., the difference between the recorded ground motions and those assessed by ground motion models for a specific earthquake). After calculating within-event residuals at recording station sites, the spatial distribution of the target intensity measure (e.g., PGA) can be estimated using the Jayaram and Baker (2009) correlation model based on global data. Residuals are equal to zero at recording station sites. The trimmed finite fault models presented in Galadini et al. (2018) were used to calculate source-to-site distances. In this document, within-event residuals were calculated using the average of the Italy-adjusted global ground motion models by Campbell and Bozorgnia (2014), Chiou and Youngs (2014), and Boore et al. (2014). This regional adjustment for Italy is needed to capture a relatively fast attenuation with distance of the ground motion observed in Italian earthquakes (e.g., Stewart et al. 2012 and Zimmaro et al. 2018). Zimmaro and Stewart (2017) recently illustrated the effectiveness of the adoption of global ground motion models with regional adjustments for applications in Italy. More details about the approach used to estimate ground motions used in this study are provided in GEER (2017) and Zimmaro et al. (2018). An estimate of PGA amplitudes at the three selected landslide sites during the 24 August, 26 October, and October 30, 2016, mainshocks is shown in Table 2.

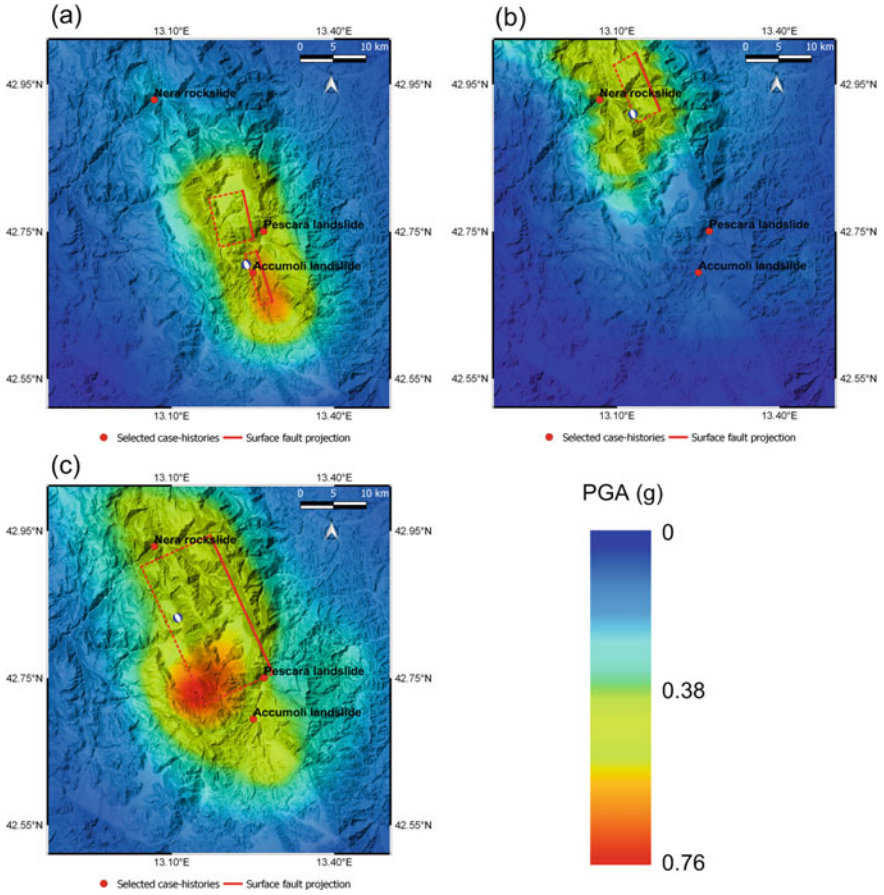


**Fig. 4** Spatial distribution of PGA (in units of g) estimated in the epicentral area for the **a** M6.1 24 August, **b** M5.9 26 October, and **c** M6.5 30 October events

**Table 2** PGA (in units of g) estimated at the selected mass-movement sites

Lat	Lon	PGA (g)			Location summary	Triggering event
		M6.1 24 August	M5.9 26 October	M6.5 30 October		
42.92900	13.06800	0.22	0.36	0.38	Nera Rockslide	M6.5, 10/30/2016
42.75057	13.27010	0.48	0.10	0.34	Pescara del Tronto	M6.1, 08/24/2016
42.69442	13.25029	0.55	0.07	0.40	Accumoli	M6.1, 08/24/2016



### 3 Rainfall Before and During the Earthquake Sequence

Three rain gauges are operated in the area affected by landslides/rockfalls: Endesa (Visso) and Ponte Tavola (Castelsantangelo Sul Nera) operated by Servizio Idrografico—Regione Marche and Nerito-Crognaleto operated by Servizio Idrografico—Regione Abruzzo. Figure 5 shows the precipitation recordings in these gauges over the time-period of the event sequence (August to December 2016). The analysis of the rain gauge recordings shows that the precipitation that occurred before the 24 August event was not significant. The largest amount of rain was recorded between August and October. However, as further discussed in the remainder of the document, none of the landslide features observed after the October events is related to rain effects.

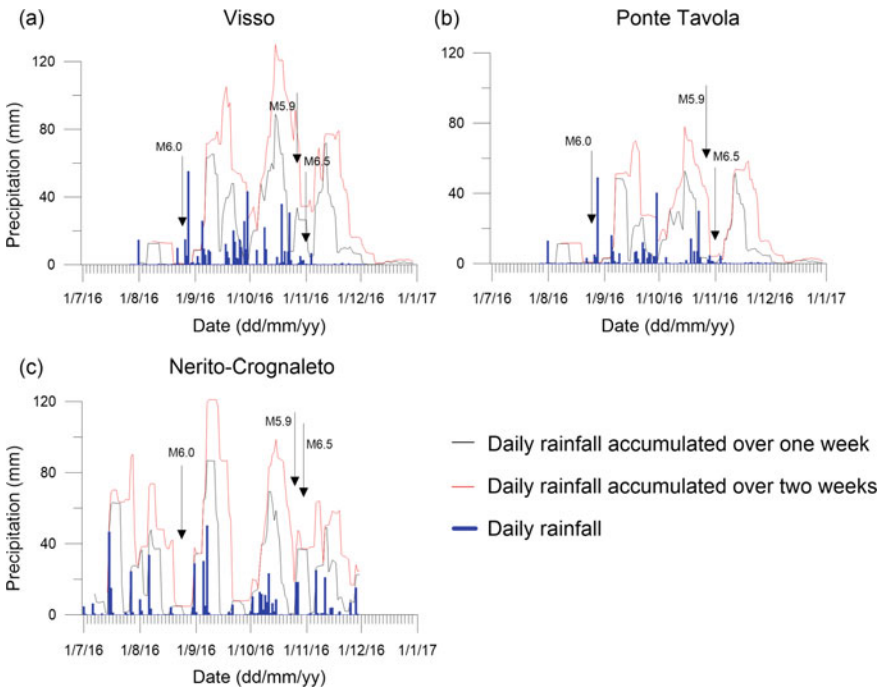


**Fig. 5** Daily rainfall (blue bars) and daily rainfall accumulated over one (black line) and two weeks (red line) recorded by rainfall gauges at **a** Visso, **b** Ponte Tavola (courtesy of Servizio Idrografico—Regione Marche), and **c** Nerito-Crognaleto (courtesy of Servizio Idrografico—Regione Abruzzo) (modified from GEER 2016)

## 4 Landslide Data

Many landslide sites are located in areas with rugged and/or steep terrain, heavy vegetation, and/or limited site access. As a result, for the GEER (2016, 2017) reports, small Uninhabited Aerial Systems (sUAS) have been extensively used to digitally image several significant landslides (Franke et al. 2018). Traditional on-site field reconnaissance investigations have also been conducted at several locations when road access was possible. Following Hungr et al. (2014), which updated the well-known Cruden and Varnes (1996) classification, landslides in the area can be classified as (Franke et al. 2018):

- (1) Rockfall and rock slides (rock planar- and rock wedge-slides involving the Miocene flysch and carbonatic units of the Umbria-Marche Succession),
- (2) Shallow translational and rotational soil slides in natural slopes such as cliffs, gulley banks, and steep natural slopes,
- (3) Shallow soil slides in anthropogenic slopes (e.g., steep roadway cuts and fills).

The information published in this document follows consistent description convention and categories. The landslides inventory was divided into three main categories as defined by Keefer (1984):

- (1) Category I: falls and slides,
- (2) Category II: coherent slides,
- (3) Category III: lateral spreads or flow slides

No features belonging to Category III were observed during the 2016 Central Italy earthquake sequence. When observed landslides do not fit any of the standard categories or are not adequately described, they are labeled as “*other*” category. Consequently, the landslides during the three main events of the seismic sequence are described as follows:

### 4.1 Landslides Following the August 24, 2016 Event

Several landslides were observed following the 24 August mainshock. Figure 6 shows mapped slope instability locations. Table 3 and Fig. 7 summarize the percentage of landslides falling into each category and the different types of landslides for each category, following the 24 August event. Most of the observed phenomena were accompanied mainly by small rockfalls along roadway cuts throughout the earthquake zone. Therefore, they fall in Category I.

The area is characterized by the presence of the following geologic units of the Umbria-Marche Succession: the Miocene flysch units and the Carbonatic units. The former comprises the so-called Laga formation, which is a flysch unit consisting of alternating sandstone (which is the prevailing component) and marl layers. Such flysch units, similarly to other turbidite formations, are characterized by variations

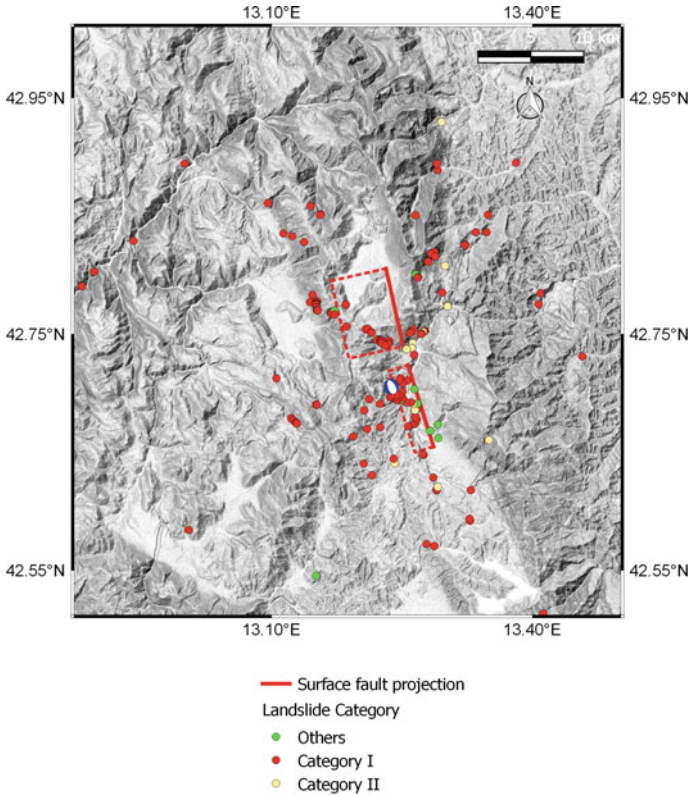


**Fig. 6** Observed landslides following the M6.1 24 August event

**Table 3** Categories of landslide occurred following the 24 August event

Category I	Category II	Other
83.1%	9.6%	7.3%
Rockfall 95%	Debris slide 71%	
Rock slide 5% (7/148)	Rock slide 29% (5/17)	

in the sandstone/marl ratio and layer thickness. This spatial variability is related to the distance from the source area in the depositional basin. The latter (marl layers) are subjected to weathering but only at shallow depths. As a result, these marls appear weathered when they are exposed (e.g., in highway cuts and excavations). This weathering undercuts overlying sandstone slabs, which can break free if shaken by earthquake ground motions.

The most impressive rockfall features were observed in the area along state provincial routes SP64 (Tufo–Castelluccio) and SP477 (Castelluccio–Norcia). Almost all of the rockfalls occurred when isolated blocks of limestone detached from outcropping bedrock above the highway. Many of these blocks came to rest on the shoulder

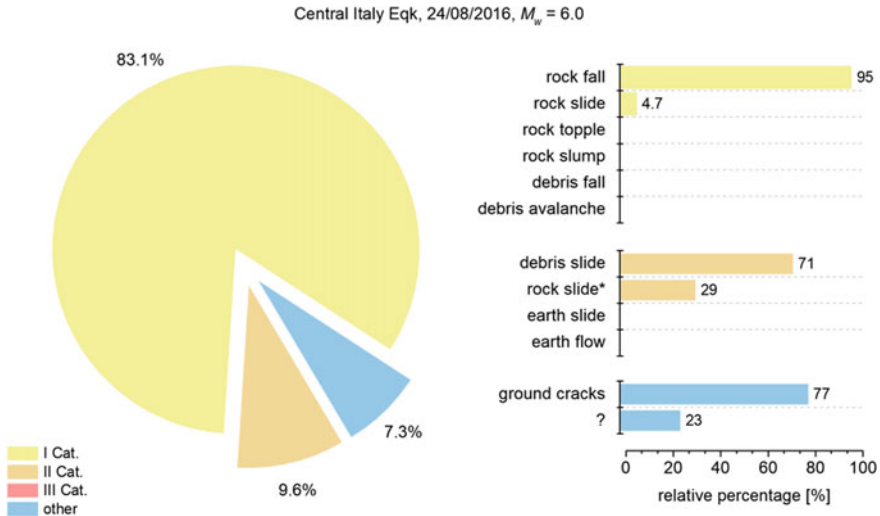


**Fig. 7** Distribution of recognized landslides after the 24 August event

or pavement of the road, whereas other blocks maintained enough velocity to cross the road and continue their descent downslope. An example of isolated blocks on highway SP477 is shown in Fig. 8a, b. Figure 8c shows an image of the 3D model developed for the SP477 rockfall using sUAS-based imagery (GEER 2016). The data collected about Category II mainly concern rock slides in gentle slopes (labeled as “rock slide”) and other phenomena referred to as “debris slide”. Many ground cracks were reported along road embankments and landfills, mainly behind retaining structures.

Figure 9 illustrates the information concerning landslides triggered by the 24 August event compared with the empirical upper-bound limits defined by Keefer (1985). Herein, the epicentral distance (Fig. 9a) and Joyner and Boore distance (the closest distance to the surface projection of an extended fault) (Fig. 9b) were plotted against the Richter surface-wave magnitude (equal to six for the 24 August event). Furthermore, Fig. 9c compares the envelope of the area affected by landslides against the upper bounds proposed by Keefer (1984) as well as those by Rodriguez et al. (1999).

The same information is illustrated in a planar manner in Fig. 10 where the areal distribution of landslide sites is compared with the empirical upper-bound loci as defined by Keefer (1985) by using two source-to-site distance metrics: epicentral distance (Fig. 10a) and the Joyner and Boore distance (Fig. 10b).

When comparing the data against empirical limits (Fig. 9), it is evident that the zone characterized by the Category I landslides is limited by the radius of 40 km around the epicenter. This extent of radius corresponds to about 50% of the upper-bound distance proposed by Keefer (1985) for this category. The majority of the

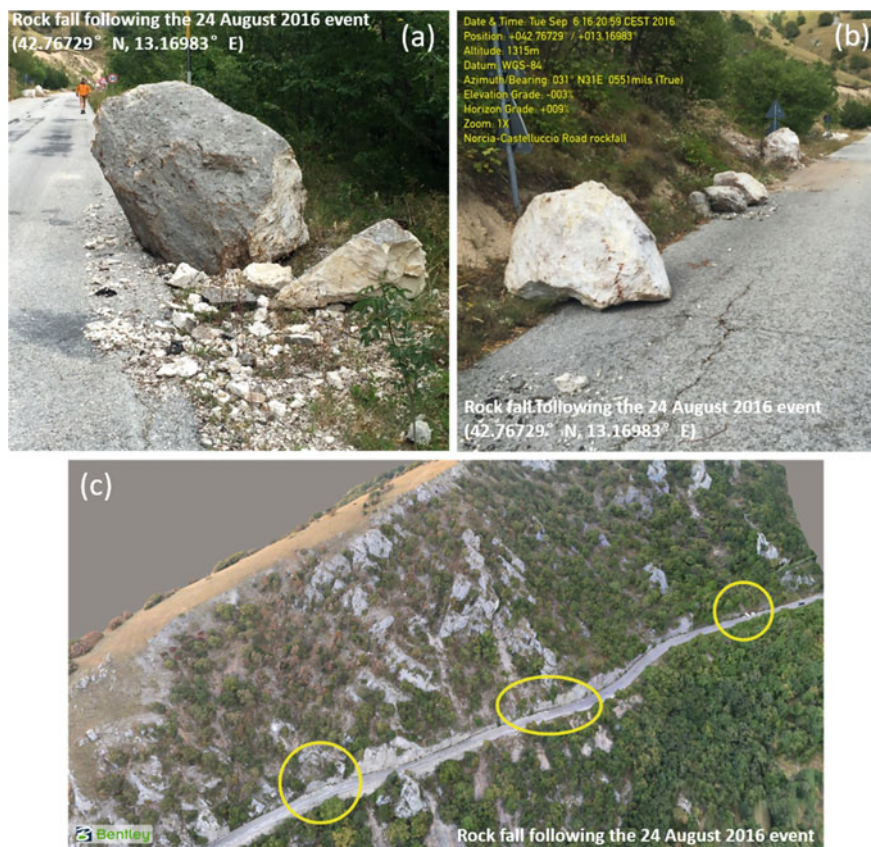


**Fig. 8** Example of rockfalls on SP477 (42.76729° N, 13.16983° E): **a** A large 2-m block of limestone that crossed the road and came to rest on the downslope side of the roadbed below a prominent outcrop of limestone (42.76729° N, 13.16983° E); **b** several blocks with sizes up to 3–4 m; **c** 3D model of the area (modified from GEER 2016)

observed landslides were located at a distance of 10 km or less from the earthquake surface ruptures. By comparing mapped landslides with the Italian landslide inventory (Inventario dei Fenomeni Franosi in Italia, IFFI project, ISPRA—Dipartimento Difesa del Suolo Servizio Geologico d' Italia, available at <http://www.progettoiffi.isprambiente.it>), it is found that the new landslides occurred mostly within the near-source zone (<10 km), while most of the far-field landslides come from the pre-existing inventory (Pavlidis et al. 2017).



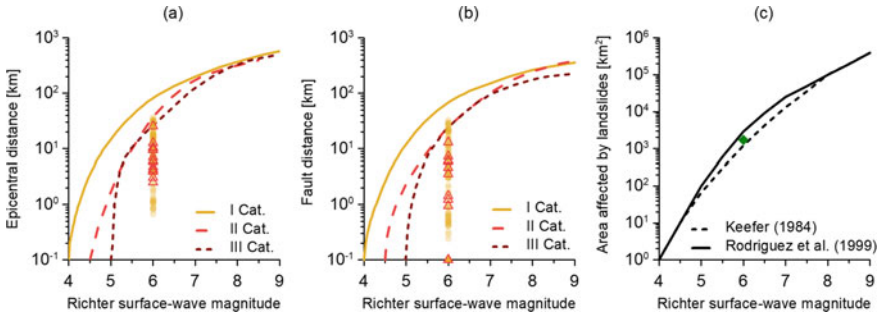


**Fig. 9** Comparison between source-to-site distances for landslides that occurred during or after the 24 August event and the empirical upper-bound curves proposed by Keefer (1985) in terms of **a** epicentral distance and **b** Joyner and Boore distance; **c** comparison between the envelope area affected by landslides and the upper bound proposed by Keefer (1984) and Rodriguez et al. (1999)

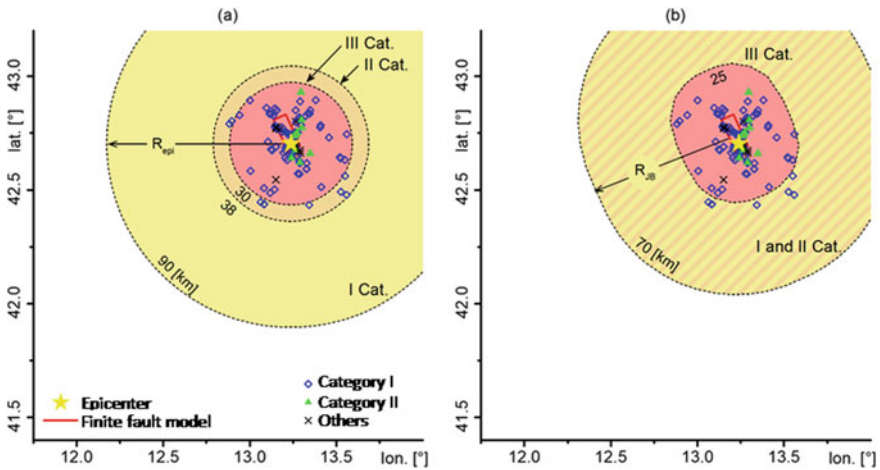


**Fig. 10** Areal distribution of landslide sites during or after the 24 August event compared with the empirical upper-bound loci defined from Keefer (1985) for two source-to-site distance metrics: **a** epicentral distance and **b** Joyner and Boore distance

### 4.2 Landslides Following the 26 and October 30, 2016 Events

The October mainshocks triggered a larger number of landslide phenomena than the 24 August mainshock. These events also exacerbated the amount of displacement caused by the 24 August earthquake event in many areas. The types of instabilities are the same as those observed following the 24 August event. Figures 11a, b shows all slope instabilities following the 26 and 30 October event, respectively. Tables 4, 5 summarize the percentage of landslides falling into each category and the different types of landslides for each category following the October events. Figure 12 shows a



graphical representation of the same information for the 30 October event. Similarly to what observed after the 24 August event, most of the observed phenomena fall in category I and involve rockfalls.

Several rockfalls observed following the October events are characterized by the large volumes of material involved. The most impressive features observed following the 26 October event are probably the series of rockfalls in the area of Mt. Bove, 4 km east-southeast of Ussita. The northern flank of Mt. Bove is characterized by massive or coarsely bedded Jurassic limestones of the Calcare Massiccio Formation.

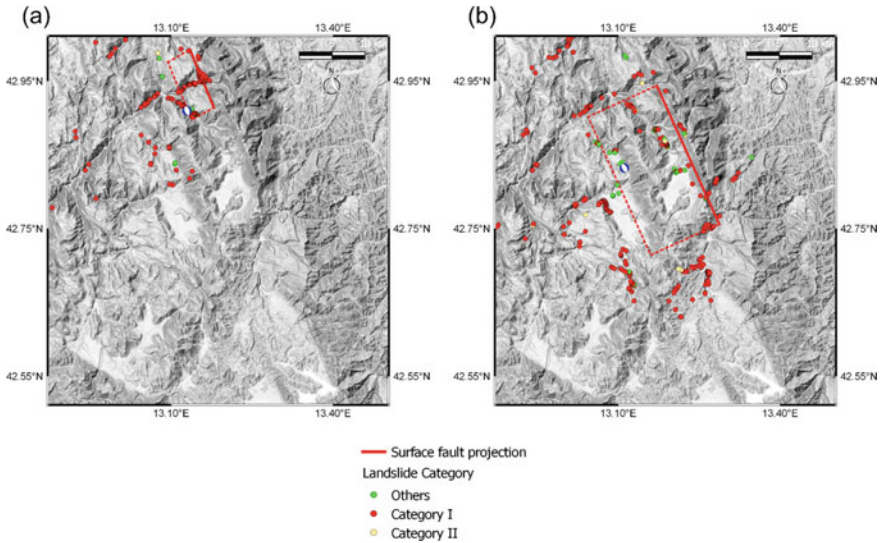


**Fig. 11** Observed landslides following the: **a** M5.9 26 October and **b** M6.5 30 October events

**Table 4** Categories of landslides that occurred following the 26 October event

Category I	Category II	Other
83%	10%	7%
Rockfall 95% Rock slide 5%	Debris slide 71% Rock slide 29%	

**Table 5** Categories of landslides that occurred following the 30 October event

Category I	Category II	Other
83%	4%	13%
Rockfall 86% Rock slide 10% Rock topple >1% Rock slump 1% Debris fall 1% Debris avalanche >1%	Debris slide 66% Rock slide 13% Earth slide 13% Earth flow 8%	

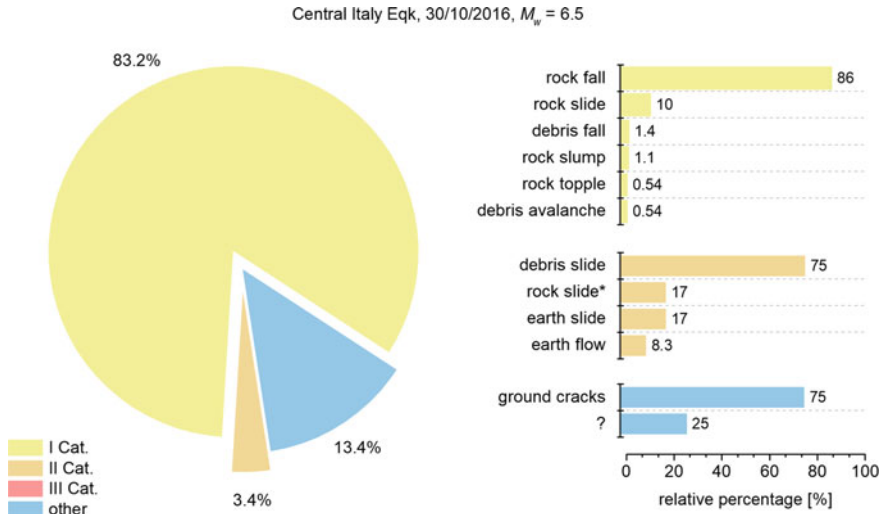


**Fig. 12** Distribution of recognized landslides after the October 30, 2016, earthquake

At the top of the mountain, the Calcare Massiccio Formation is overlaid by limestones (Bugarone Formation) with more regular bedding (medium to thick beds). The Mt. Bove massif has been involved in intense Quaternary and ancient tectonics, which has produced faults trending in a strike range from ESE-WNW to N-S. The rock mass has closely spaced joints and persistent joints belonging to the major joint sets. Sever loosening of thick outer parts of the intensely fractured mountain flank could have favored the detachment of large irregular slices under seismic loading (GEER 2017). Figure 13 shows a sUAS-based image of a talus fields visible at the base of Mt. Bove. The same figure also highlights suspected source areas for these talus fields characterized by a lighter coloration of the freshly-exposed unweathered limestone (yellow circled areas in Fig. 13).

Another interesting rockfall feature is that observed in the Valle di Panico. This instability phenomenon has been likely triggered by the 30 October event. However, this information is only inferred, since prior information about it was not available at the time of reconnaissance (Lanzo et al. 2018). Mt. Bove represents the southern flank of the narrow valley called Valle di Panico. The northern flank of this valley is formed by a succession of limestone and marly units from Jurassic to Cretaceous in age. There are two landslide locations along the mountain road that winds along the northern flank of Valle di Panico. The road is cut into thinly-bedded marly limestones (Scaglia Bianca Formation) whose bedding joints frequently have a clay/bituminous infilling. This structural/lithologic feature, together with an intense fracturing, gives the rock mass a low quality. The source area of the rockfall at the second site is located in a marly-limestone unit featured by thicker layers. In this area, the bedrock is extensively covered by slope debris that are some meters thick (GEER 2017). The GEER reconnaissance team visited two main sites in the Valle di Panico area. The first

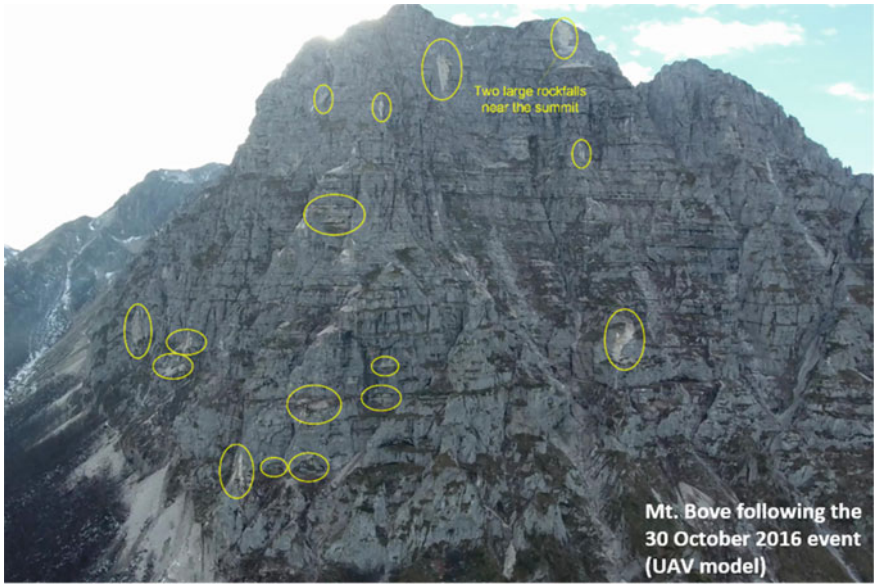


**Fig. 13** sUAS image of Mt. Bove. Suspected rockfall sources are circled in yellow (modified from GEER 2017)

site was a landslide in the soil slope through and beneath the road. Figure 14 shows an aerial photograph of this 55–60 m wide landslide. The GEER team measured a vertical offset on the road pavement ranging between 10 and 70 cm, and horizontal deformation ranging from 2 to 40 cm. The GEER team also created sUAS-based 3D models of this landslide. As shown in Fig. 15a, the eastern portion of the landslide headscarp shows distinct cracks and associated displacements. The western portion of the headscarp appears more gradual and shows pavement cracking (Fig. 15b).

The second site in the Valle di Panico area is a 420 m-long rockfall along a mountain road. Figure 16 shows a 3D model of the entire rockfall produced by



**Fig. 14** Aerial photograph of the Valle di Panico landslide (modified from GEER 2017)

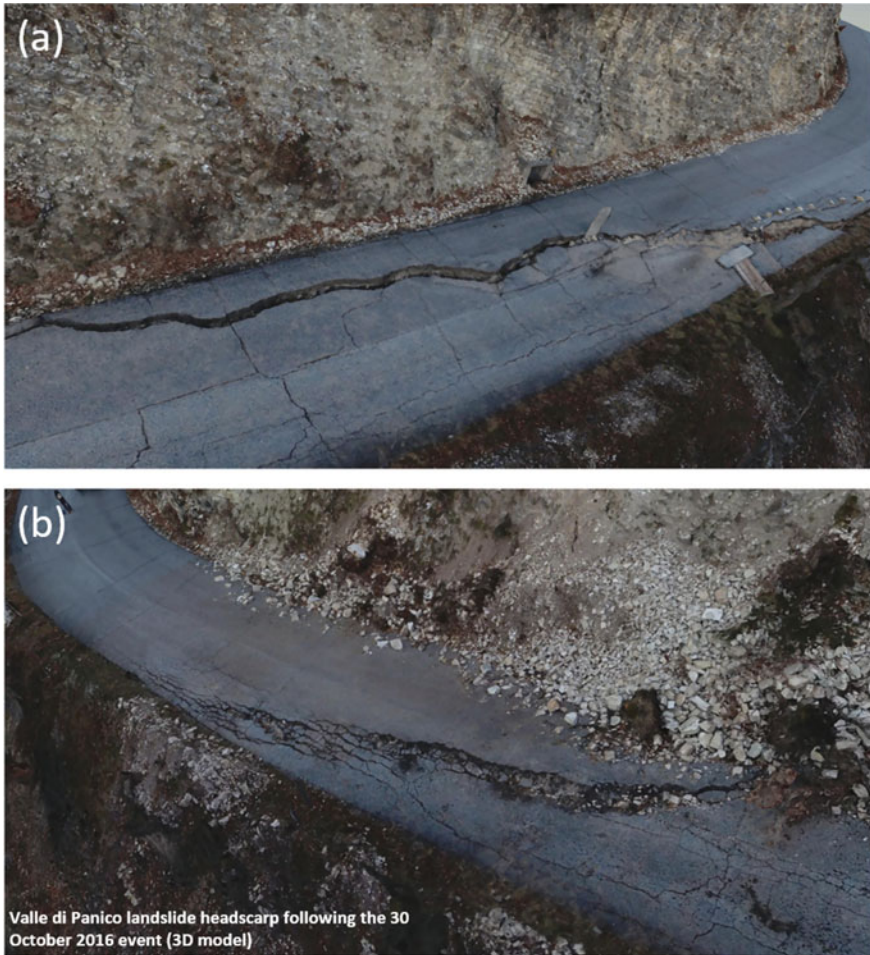


**Fig. 15** a 3D model of the eastern half of the Valle di Panico landslide headscarp; b 3D model of the western half of the landslide headscarp (modified from GEER 2017)

the GEER team (GEER 2017). The total change in elevation from the source of the boulder to the final resting place on the bottom of the valley is approximately 235 m. The side slope of the valley rests at an angle of 34 degrees from the horizontal direction (1.5 H:1 V). Numerous boulder fragments ranging in diameter from gravel-size to over 3 m were observed and photographed along the entire rockfall length. The largest boulder measures 3 m in diameter. The source boulder is 11.2 m in length and belongs to a formation of heavily weathered and fractured limestone located 91 m above the mountain road (Fig. 17a). Much of the limestone boulder exploded into gravel-sized fragments in the first 90 m of the rockfall. The remaining parts of the boulder broke in larger fragments while tumbling to the bottom of the valley





**Fig. 16** sUAS-based 3D model of the Valle di Panico rockfall (modified from GEER 2017)

(GEER 2017). At the bottom of the valley, over ten large boulder fragments ranging in diameter from 0.8 to 2.9 m were observed to rest at the valley floor, just 13 m from what appeared to be a small pump or power house (Fig. 17b). Information reported by the GEER team shows that none of the boulders appear to have damaged this small structure (GEER 2017).

Figure 18 depicts the data of landslides triggered by the 30 October event and compare it with the empirical upper-bound limits defined by Keefer (1985). For this diagram, Richter surface-wave magnitude was employed in association with the epicentral distance (Fig. 18a) and Joyner and Boore distance (Fig. 18b). Figure 18c compares the envelope area affected by landslides and the upper bounds proposed by Keefer (1984) and Rodriguez et al. (1999). The same information is also presented in a planar style in Fig. 19. It draws the areal distribution of landslide sites and compare it with the empirical upper-bound loci as defined by Keefer (1985) for two source-to-site distance metrics: epicentral distance (Fig. 19a) and Joyner and Boore distance (Fig. 19b). The comparison with the empirical limits indicates that the zone involved in the activation of Category I landslides is limited to an area with a radius of about 40 km around the epicenter, with the majority being at 10 km or less from the surface ruptures.

## 5 Landslide Detection During the 2016 Central Italy Earthquake Sequence Using Geodetic Methods

Several geodetic methods use synthetic aperture radar (SAR) images to generate digital elevation models (DEM) for monitoring ground and structural deformation.

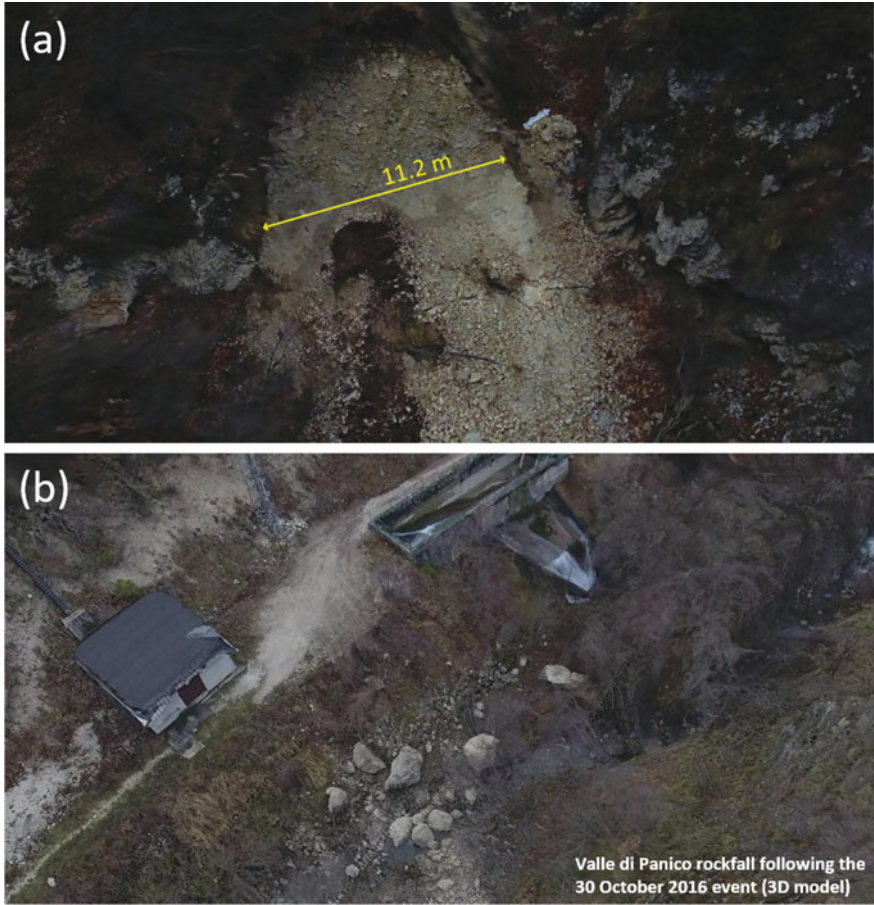


**Fig. 17** **a** 3D model of the source of the Valle di Panico rockfall, located 90 m above the mountain road; **b** 3D model of the boulders and a small power or pump house at the toe of the Valle di Panico rockfall (modified from GEER 2017)

These methods are typically based on differences in the phase of waves returning to a moving platform (e.g., aircraft or satellites). SAR-based techniques are often utilized to identify deformation phenomena such as (1) earthquake-related surface deformations and ruptures (e.g., Jo et al. 2010), (2) volcanic eruptions (e.g., Jung et al. 2011; Lee et al. 2013), (3) subsidence (e.g. Choi et al. 2011; Zhang et al. 2012), and (4) massive landslides (e.g., Ausilio and Zimmaro 2017). Such techniques have been also recently used to perform rapid detection and regional mapping of landslides following earthquakes (e.g., Rathje and Franke 2016 following the 2004 Niigata-ken Chuetsu earthquake). It is worth mentioning that satellite-based detection of ground elevation often underestimates the size of the landslides (Rathje and Carr 2010; Rathje and Franke 2016). SAR-based methods are also employed to rapidly



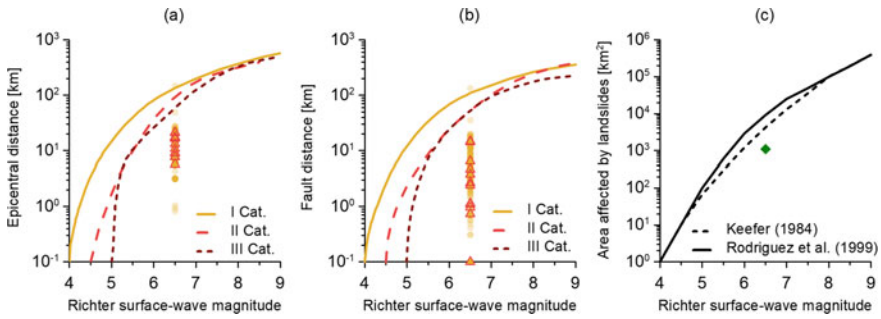


**Fig. 18** Comparison between source-to-site distances for landslides that occurred following the 30 October event and the empirical upper-bound curves proposed by Keefer (1985) in terms of **a** epicentral distance and **b** Joyner and Boore distance; **c** comparison between the envelope area affected by landslides and the upper bound proposed by Keefer (1984) and Rodriguez et al. (1999)

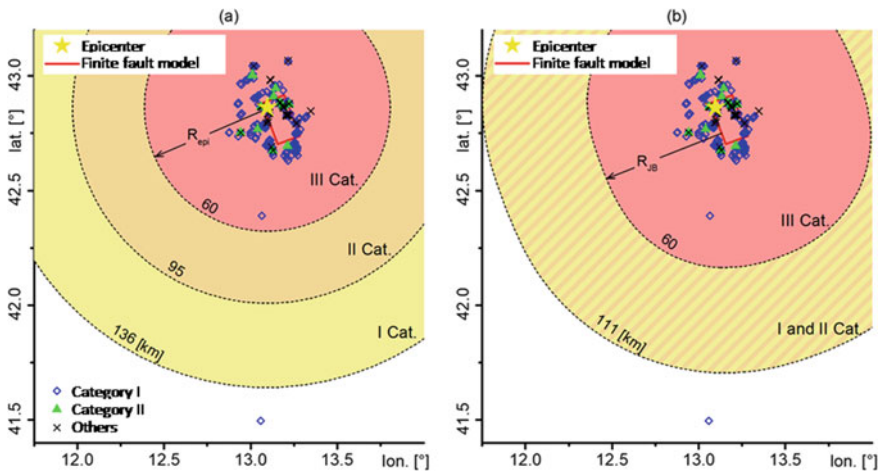


**Fig. 19** Areal distribution of landslide sites following the 30 October event compared with empirical upper-bound loci defined from Keefer (1985) for two source-to-site distance metrics: **a** epicentral distance and **b** Joyner and Boore distance

produce post-disaster deformation maps. This is one of the goals to be achieved by the Advanced Rapid Imaging and Analysis (ARIA 2016) project. The ARIA project team releases coseismic interferograms and damage proxy maps following major natural disasters globally. The damage proxy maps are produced by comparing interferometric SAR coherence maps before and after an extreme event (e.g., Fielding et al. 2005; Yun et al. 2011). Yun et al. (2015) showed that the extents of coseismic slope instability caused by selected earthquakes were well captured by damage proxy maps. Such maps have been also used to identify possible landslide and rockfall locations following the 2016 Central Italy earthquake sequence, as shown in Fig. 20, which shows clusters of coherence changes in damage proxy maps versus detected

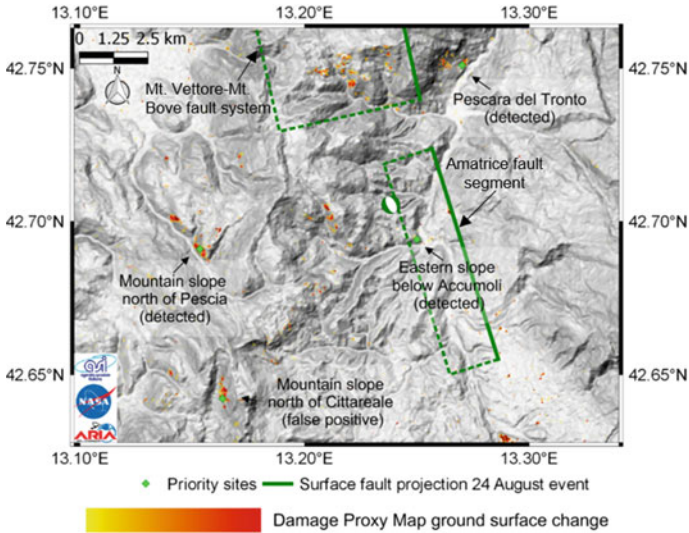


**Fig. 20** Epicentral area of the M6.1 August 24 earthquake together with damage proxy maps of the area produced by the ARIA project and detected landslide features (modified from Franke et al. 2018)

landslide features following the 21 August event (GEER 2016 and Franke et al. 2018). Also Polcari et al. (2017) used SAR data to detect instabilities in the epicentral area of the 2016 Central Italy sequence, focusing on mountainous areas.

One of the instabilities detected by Franke et al. (2018) following the 24 August event is the Pescia rockfall. Figure 21 shows the sUAS-based 3D models of the Pescia rockfall. At this location, the GEER team produced multi-epoch 3D models showing that after the detection of rockfalls following the 24 August event, additional boulders fell as a result of the 30 October event. The rock face reported in Fig. 21 is approximately 90 m wide and 60 m high. The rock material that composes the face is a combination of limestone, argillaceous limestone, and marlstone. Boulder sizes reach 2.5 m. Next to this location, the GEER team detected additional rockfalls produced by the 30 October event that were not present after the 24 August event. Figure 22 shows a 3D model of these features.

## 6 Relevant Case Histories

This section focuses on three major landslide features, judged as valuable case histories:

- (1) The south-western flank of the Nera River valley, located south-west of Visso Village, where a large rockslide was induced by the M6.5 earthquake on October 30, 2016, and is known as the Nera rockslide or Mount Sasso Pizzuto Rockfall;

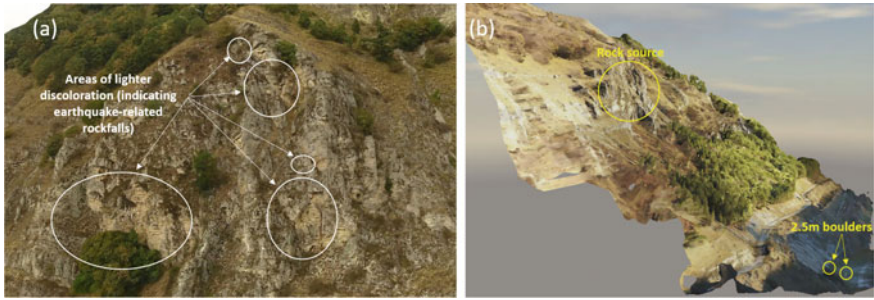


**Fig. 21** sUAS-based 3D models of the Pescia rockfall following the **a** 24 August and **b** 30 October event (modified from GEER 2016, 2017)

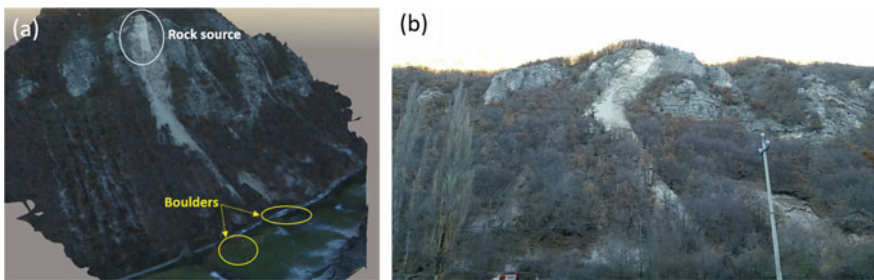


**Fig. 22** **a** sUAS-based 3D models of additional rockfall features observed in the area of Pescia following the 30 October event; **b** source area of the rockfalls with runout damage (modified from GEER 2016, 2017)

- (2) Pescara del Tronto, where the 2016 events caused significant cumulative damage in a soil/rock slope overlooking the SS4 motorway, connecting the west to the east coast of Central Italy;
- (3) Accumoli, where slope failures occurred on the southern spur of the hill on top of which the village is built.

GEER reports (2016, 2017) showed that incremental accumulation of the structural damage was especially intense in Pescara del Tronto and Accumoli. The damage accumulation at these and other locations is related with the multiple cycles of mainshock-aftershock sequences observed in the area between August and October 2016. Additional information about these selected case histories are presented by Lanzo et al. (2018). Figure 23 shows the location of these case histories, along with epicenters of the three mainshocks of the sequence.

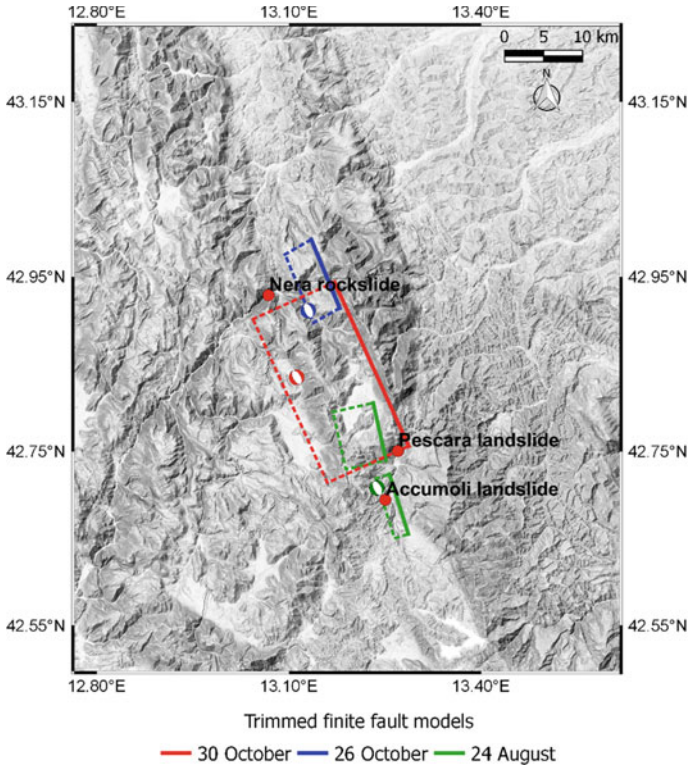


**Fig. 23** Location of selected case histories

### **6.1 Nera Rockslide or Mount Sasso Pizzuto Rockfall**

The Nera River Valley is a huge canyon formed by the erosion of the Nera River, a tributary of the Tiber River, in limestone formations between the Umbria and Marche regional border (Fig. 24). In some stretches, the regional road (SP 209) runs along the Nera River. The Italian landslide inventory (Inventario dei movimenti franosi in Italia, IFFI project, ISPRA Dipartimento Difesa del Suolo Servizio Geologico d'Italia) classifies this area as being subject to rockfalls and slumps. The geology in the Nera River valley area is characterized by sedimentary rocks of the carbonate Umbria-Marche stratigraphic sequence, which is an early Jurassic to Eocene age formation. The geology of the area (Romeo et al. 2017) is also associated with the outcropping of bedrock of the Umbria-Marche sequence between Calcare Massiccio (a massive platform limestone) and Scaglia Variegata-Cinerea (marly-calcareous rocks). The Maiolica Formation (stratified pelagic limestone) is present in the left bank of the Nera River. In some parts, the formations are pervasively folded (crumpled) and intensely fractured (Romeo et al. 2017).

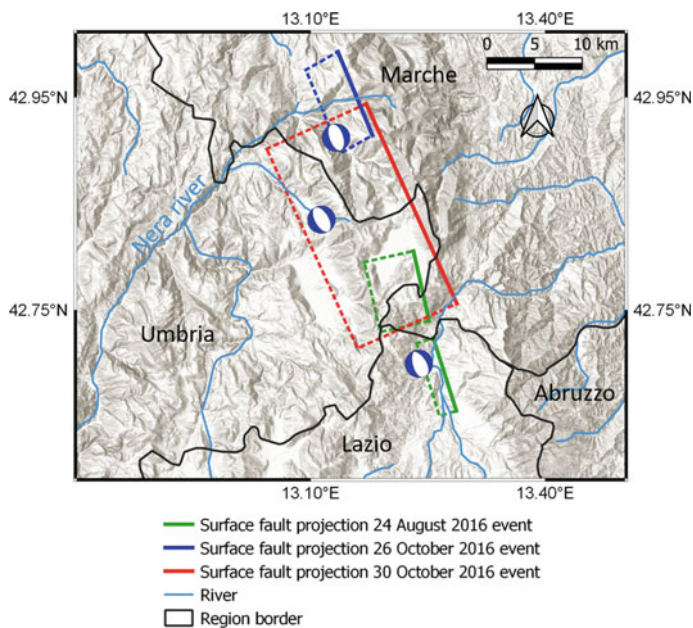


**Fig. 24** Location of the Nera River area between the Umbria and Marche regional border

Several rockfalls and diffuse instabilities occurred along this valley during the 2016 Central Italy earthquake sequence. Very few and small landslides were triggered by the 24 August event, while severe rockfalls occurred following the October 2016 events. Boulders, with a volume ranging from a dozen cubic centimeters to a few cubic meters, have been observed on the shoulders and/or across the road. Figure 25 shows cases in which the installed rockfall protection measures were passed over, severely damaged or destroyed. These passive protection measures (i.e., rockfall nets, dynamic rockfall barriers, rigid barriers, or catch fences) were built along the SP 209 stretch after the 1997 Umbria-Marche earthquake sequence, which triggered about 200 rockfalls of various sizes along the Nera River Valley, and damaged man-made infrastructure such as roads, bridges, and tunnels (Carro et al. 2003; Gigli et al. 2014).

The largest and most important rockfall occurred following the 30 October earthquake, 1 km south-west of Visso, along the steep-faced north slope of Mount Sasso Pizzuto, which is characterized by highly deformed, stratified, and fractured rocks (Maiolica Formation). The avalanche generated by this rockfall interrupted the regional road (SP 209) and dammed the Nera River, forming a small lake of about 2000 m<sup>2</sup>. This feature is known as the Nera rockslide or Mount Sasso Pizzuto rockfall. This rock avalanche affected the road transportation between Visso and the town of Terni (center of the administrative and industrial activities in the Umbria region) and the transportation network within the whole Central Apennine. Fish farming activities, which is a source of the significant financial income of this area, were damaged by the avalanche deposit as well. The presence of such fish farming activities, along





**Fig. 25** Slope protection damaged by boulders and rock-blocks along the regional road SP 290 in the Nera River valley (modified from GEER 2017)

with obvious environmental concerns, imposed a need for extra care in the removal of the landslide dam, making this operation very lengthy. Detailed geometric information can be found in the report by GEER (2017) and in Romeo et al. (2017). In both documents, for safety reasons, remote-sensing measurement techniques have been used without direct site inspections in the landslide area. Table 2 showed that the estimated PGA value for the 30 October event at this location is 0.38 g (GEER 2017; Zimmaro et al. 2018; Franke et al. 2018).

The geometry of the rockslide scar and the avalanche deposit were quantitatively measured by photogrammetric reconstruction of images captured by sUAS flights at the beginning of December, 2016, by GEER (2017). The Structure-from-Motion (SfM) computer vision was employed for post-processing and geo-referencing of the acquired sUAS data in order to reconstruct a 3D image (more details in GEER 2017). The resulting 3D model is shown in Fig. 26. Figure 27 shows details of the talus damming the Nera River (Franke et al. 2018). Romeo et al. (2017) have used a TruPulse™ 200 laser rangefinder. The laser sensor was placed on a tripod in order to carry out the measurement of slope distance, horizontal and vertical distance, and inclination, or the calculation of the elevation of any target. Thirty points were installed on the landslide debris that covers an area of about 16,500 m<sup>2</sup>. Furthermore, GIS analysis was defined in ArcGIS 10.1 (more details in Romeo et al. 2017).



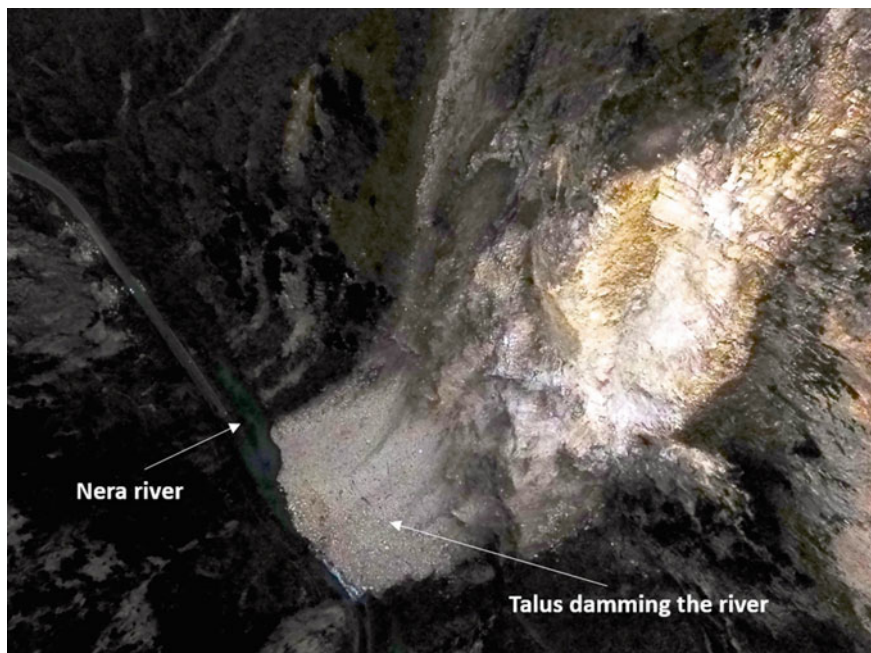


**Fig. 26** Nera rockslide photographed by the GEER sUASat at an elevation of 400 m above Route SP 209. The primary rockfall was a wedge that detached on the right side of the image and disintegrated into talus debris as it fell 330 m to the river valley floor. The limestone bedding is visible in the scar of the wedge detachment (modified from GEER 2017)

The maximum elevation difference between the rockfall source area, close to the ridge of the slope, and the SP209 road is about 300 m. The slope angle at the detachment area was originally greater than  $58^\circ$ , while after the detachment is between  $75^\circ$  and  $80^\circ$ . The rockslide scar can be approximated by those left by a rock wedge delimited by two persistent joints and the cliff surface, as can be seen in the SfM imagery of Fig. 27. The bedding exhibits an apparent dip of  $20^\circ$ – $30^\circ$  toward the east and appears to be orthogonal to the joints delimiting the failed wedge, thus it did not play a major role in the sliding mechanism. The apron of debris accumulation has a slope angle of about  $27^\circ$  and is not exactly in the perpendicular direction from the source. The accumulation area covers the foot of the slope and has an extent of about  $20,000 \text{ m}^2$ . It is difficult to determine the volumetric ratio of the materials derived from the source area and that from the pre-existing debris along the slope. Romeo et al. (2017) have estimated the total volume (debris originated by the rockfall plus the mobilized pre-existing talus) at about  $70,000 \pm 8000 \text{ m}^3$ , of which about  $50,000 \pm 60,000 \text{ m}^3$  is derived from the new event. This estimate is comparable to the volume of rock detached from the source area (about  $40,000 \text{ m}^3$ ) determined by laser rangefinder, taking into account the considerable uncertainties in evaluating the pre-existing material. Similar conclusions on pre- and post-event talus deposits

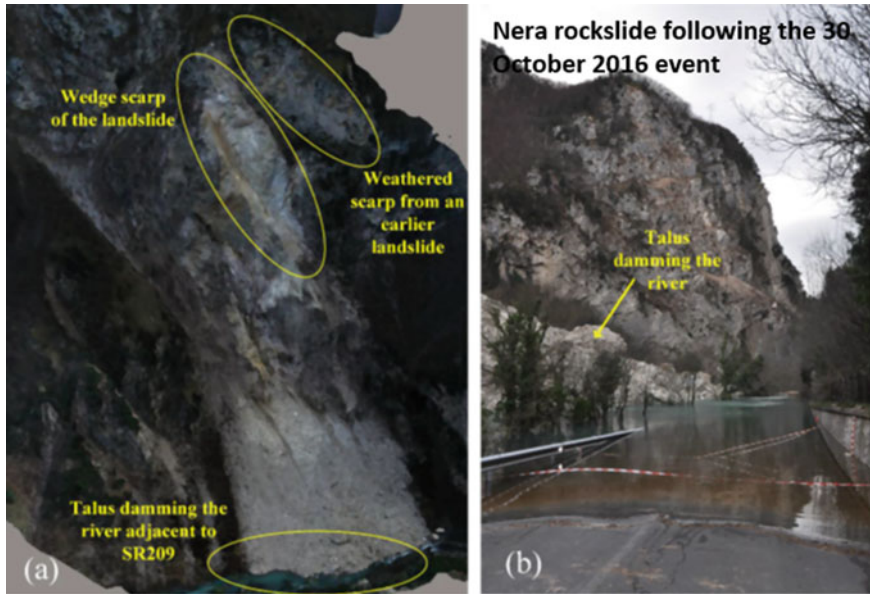


**Fig. 27** **a** 3D model of the Nera rockslide; **b** photograph of the dammed Nera River blocking the road (modified from Franke et al. 2018)

have been reached by Franke et al. (2018) using sUAS-based 3D models. It is not a particularly large slope failure, but probably is the biggest rockfall in the area during the last two centuries.

## 6.2 Slope Displacements in Pescara Del Tronto

Significant incremental ground deformations were observed in the village of Pescara del Tronto following the 24 August event (GEER 2016) and the October events (GEER 2017). For safety reasons, measurement techniques have been used without a direct approach to the landslides areas after the 24 August and 30 October events. A series of sUAS flights have been made to collect aerial imagery over the areas of interest due to landslides. sUAS-based photographs were subsequently processed with a SfM computer vision algorithm using Bentley ContextCapture software and Pix4D software to develop orthophotos and 3D point's clouds and meshed models. Additional details about these indirect measurement techniques are provided by Franke et al. (2018).

The village suffered very heavy damage, with many masonry building collapses and 48 fatalities on 122 inhabitants during the 24 August event. This village together with all the downtown of Amatrice and Petrana was characterized by the highest intensity 10–11 MCS (Mercalli-Cancani-Sieberg scale; Sieberg 1930) (Galli et al.

2016) during the sequence. A structure-by-structure damage assessment for Pescara del Tronto following the 24 August and 30 October events is given in Sextos et al. (2018).

The village of Pescara del Tronto is located at the foot of the southern escarpment of Mt. Vettore, downslope from the so-called Sibillini thrust. In this zone, the Umbro-Marchigiana carbonate sequence overlaps the Laga formation. Pescara del Tronto is built on a slope comprising pre-existing ancient landslide deposits. These deposits consist of angular carbonate clasts ranging in size from sands to cobbles, with interspersed pervasively fractured limestone blocks. The deposits thickness varies spatially, thinning when proceeding toward the slope foot (the Tronto River left bank). In this zone, they overlie fluvio-lacustrine sediments, including travertines. The bedrock is the turbiditic Laga Formation. In the cataclastic carbonate rocks, distributed along the thrust line, which are located a few hundred meters upslope from the Pescara del Tronto village, it is possible to observe a large landslide crown (at elevations ranging between 900 and 1150 m above the sea level). This complex configuration was likely generated by the coalescence of various rotational-translational and complex landslides. Some evidence of this complexity are the benches, counter-slopes, and high scarps still present along the slope. These landslides are probably the source of thick debris deposits that the village of Pescara del Tronto is built on (Aringoli et al. 2010 and Lanzo et al. 2018).

After the August events investigation of the 3D models of Pescara del Tronto produced by the GEER team (GEER 2016, 2017) revealed numerous shallow earthquake-induced landslides and retaining wall failures. The remainder of this section summarizes incremental slope instability features observed as a result of the 2016 Central Italy earthquake sequence. This analysis is largely based on multi-epoch observations mainly derived from sUAS-based 3D models. Seven locations of interest within Pescara del Tronto have been identified to carry out cumulative damage analysis (Fig. 28; GEER 2016, 2017).

The largest landslide occurred on the east slope below the city ( $42.75057^\circ$  N,  $13.27223^\circ$  E), directly above Highway SS4 (marked as #1 in Fig. 28). The landslide after the 24 August event was approximately 75 m wide and 30 m high, and was shallow, with only the upper one meter or less of soil sliding downslope. The landslide damaged retaining structures around the city. Significant incremental movements occurred on the landslide above highway SS4 after the two October events as shown in Fig. 29a, b. Limestone boulders greater than 6 m in diameter were detached from the slope and rolled onto the highway.

A second, smaller shallow landslide was located above Highway SS4 (marked as #2 in Fig. 28), just south of the larger landslide #1 ( $42.7501^\circ$  N,  $13.2719^\circ$  E). This landslide was approximately 16 m wide and occurred on a slope 26 m high. Figure 30 shows a comparison between 3D models produced for this feature following the 24 August and 30 October events. This smaller landslide was not observed to change significantly after the 24 August event (Fig. 30a) and the 30 October earthquake (Fig. 30b). In this section, the retaining wall supporting the road appeared to maintain its stability. However, significantly more structural debris from collapsed residences was observed at this location following the 30 October earthquake.



**Fig. 28** 3D model of Pescara del Tronto following the 24 August event. Yellow circles highlight the seven locations discussed in this document (modified from GEER 2017)

A few of the observed slope failures in Pescara del Tronto appear to be related to potential retaining wall failures. The lower portion of Pescara del Tronto was partially supported by a 24 m-tall masonry retaining wall that surrounded the foot of the village. This wall suffered serious damage following the 24 August event (Fig. 31a). Substantial damage accumulation was observed following the October events as shown in Fig. 31b. In Pescara del Tronto, structure debris was so ubiquitous that it was challenging to investigate ground deformation in this zone. Any attempt to directly investigate this zone was not realistic because of the dangerous and unstable nature of the debris field. As a result, sUAS-based imagery constituted the main damage detection and analysis tool, especially after the October events. Moderate to severe damage was found along most of the roads in proximity from the slopes and/or above the retaining walls throughout Pescara del Tronto.

Figure 32a shows a minor sloughing of the gully wall observed following the 24 August event from sUAS-based imagery (feature #5 in Fig. 28). In the same area, sUAS-based imagery captured following the October earthquake events shown that a section of the slope nearly 9 m thick and 20 m wide failed into the gully (Fig. 32b). The remaining scarp is nearly 12 m in height and stands at an angle of 52 degrees, remarkably similar to the same scarp angle that remains behind the failed lower retaining wall (i.e., Areas 3 and 4). A small residential structure that was observed



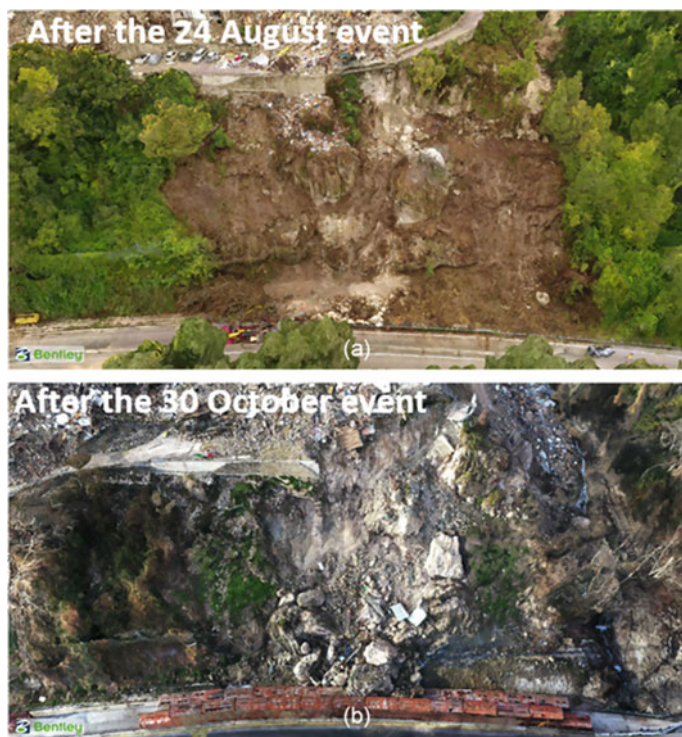


**Fig. 29** D model of landslide #1 in Pescara del Tronto following: **a** the 24 August and **b** the 30 October event (modified from GEER 2017)

to rest on top of the slope after August event had plummeted into the gully after the October event.

Another shallow landslide occurred on the northern side of Pescara del Tronto (marked as #6 in Fig. 28) following the 24 August event (Fig. 33a). This landslide is approximately 17 m wide by 20 m high. A significant amount of structural rubble from collapsed residences is also visible in the landslide debris. Additional observations carried out following the October events revealed that the depth of the landslide remained relatively unchanged, but its width expanded from 17 m to more than 36 m (Fig. 33b). In both cases (following the 24 August and the October events), landslide sizes have been measured using sUAS-based imagery (GEER 2017).

The last landslide feature present in the area of Pescara del Tronto is located on the slope bounding the gravel pit on the southern upper portion of the village adjacent to the SP 129 highway (marked as #7 in Fig. 28). Observations made following the 24 August event show that the gravel pit is approximately 70 m by 90 m, and has 2.4 V:1H side slopes comprised of slightly cemented cataclasized limestone blocks interspersed in a gravelly-sandy matrix comprised of angular limestone clasts (Fig. 34a). A dirt haul road extending up and along the edge of the slope is located on





**Fig. 30** 3D model of the landslide #2 in Pescara del Tronto following: **a** the 24 August and **b** the 30 October event (modified from GEER 2017)

the south side of the gravel pit. The landslide exposed about 15 m of a 50 cm-diameter pipeline that was shallowly buried beneath the dirt haul road. The shape and size of the landslide remained almost unchanged following the October earthquake events as shown in Fig. 34b. However, the slope beneath the haul road degraded slightly more, causing nearly half of the haul road above the landslide to disappear. Approximately 8 more meters of the pipeline became exposed from the additional slope movements, causing the pipeline to apparently sag and bow slightly. Another smaller pipe of a few centimeters' diameter was also exposed and sagging substantially along the scarp.



**Fig. 31** 3D model of the failed retaining wall area in Pescara del Tronto (areas #3–4 in Fig. 28) following: **a** the 24 August and **b** the 30 October event (modified from GEER 2017)

### 6.3 Slope Displacements in Accumoli

Accumoli is a small village in the Rieti province, located atop the elongated WNW-ESE ridge with its elevation ranging from 860 to 890 m a.s.l. (Fig. 35). The geology in this area is underlain by the Laga Formation as the bed rock and is mainly composed of arenaceous materials. This formation, whose shallow parts are often loosened and weathered, is locally covered by colluvium and landslide deposits. The village is located in the epicentral area of the August 24, 2016, mainshock. Accumoli suffered damage during the January 14, 1703, Valnerina earthquake (M6.9). Zimmaro et al. (2018) estimated a  $PGA = 0.40$  g during the 30 October event and a  $PGA = 0.55$  g during the 24 August event in Accumoli (Table 2). Structural and landslide-related damage observed following the October events (GEER 2017) was significantly more serious than that observed after the August event and was documented by GEER (2016).

We analyze landslide-related damage that occurred in two zones: (1) Point A in Fig. 35: incremental damage to a retaining wall, and (2) Point B in Fig. 35, a shallow slope failure on the eastern side of the village. Following the 24 August event, a



**Fig. 32** 3D model of the failure observed in area #5 in Fig. 28 following: **a** the 24 August and **b** the 30 October event (modified from GEER 2017)

4.8 m-tall retaining wall located at the eastern tip of the spur was observed to have rotated outwards 3.6 degrees, with horizontal movements of 57 cm and downward vertical movements of nearly 18 cm. A soil graben nearly 2.7 m wide was observed behind the rotated wall, with soil settlements of 45–50 cm. Much more damage was observed following the October events. It is thus supposed that a shallow landslide developed beneath the retaining wall and caused the entire structure to slide down over several meters along the slope.

Figure 36 presents an aerial screenshot of the 3D model developed from sUASim-ery of the site, showing evident incremental damage as a result of the earthquake sequence. The shallow landslide appeared to be limited to the upper corner of the slope, near the crown. The slide, therefore, likely occurred in the man-made fill slopes that was placed during the construction of the village. The scarp of the landslide appeared to follow the scarp of the soil graben observed behind the wall following the 24 August event, suggesting that the graben may have been caused not necessarily by the rotation of the retaining wall alone. The landslide displaced the top of the wall by 5–6 m in the horizontal direction and between 3 and 4 m in the downward vertical direction. In total, approximately 50 m of the retaining wall failed and slid 5–6 m





**Fig. 33** 3D model of landslide #6 following: **a** the 24 August and **b** the 30 October event (modified from GEER 2017)

downslope. Further, south at Point A, a series of shallow cracks (orthogonal to the dip of the slope) approximately 5–14 cm in width were observed following the 24 August event. These cracks extended after the October events up to a width ranging between 80–190 cm. The depth of the cracks was approximately 55 cm.



**Fig. 34** 3D model of landslide #7 and exposed pipeline following: **a** the 24 August and **b** the 30 October event (modified from GEER 2017)





**Fig. 35** Accumoli map with locations of the landslide-related damage observed during the August and October events (modified from Lanzo et al. 2018)



**Fig. 36** 3D model screenshots following: **a** the 24 August and **b** 30 October event (modified from Lanzo et al. 2018)

## References

Advanced Rapid Imaging and Analysis (ARIA)—Center for Natural Hazards (2016) ARIA Data Share Available at: <https://aria-share.jpl.nasa.gov/>. Last Accessed 26 September 2017

Ambraseys NN (1976) The Gemona di Friuli earthquake of 6 May 1976. UNESCO Restricted Technical Report, RP/1975–76/2.222.3, Part II

Antonini G, Ardizzone F, Cardinali M, Galli M, Guzzetti F, Reichenbach P (2002) Surfaces deposits and landslide inventory map of the area affected by 1997 Umbria-Marche earthquakes. *Boll Soc Geol It* 1:843–853

- Aringoli D, Gentili B, Materazzi M, Pambianchi G (2010) Mass movements in Adriatic Central Italy: activation and evolutive control factors. In: Werner, Friedman (eds) *Landslides: causes, types and effects*. Nova Science Publishers, Inc. New York, NY, USA, pp 1–71
- Ausilio E, Zimmaro P (2017) Landslide characterization using a multidisciplinary approach. *Measurement* 104:294–301
- Ausilio E, Silvestri F, Tropeano G, Zimmaro P (2019) Spatial distribution of landslides triggered by the 2016 Central Italy seismic sequence. In: Silvestri, Moraci (eds) *Earthquake geotechnical engineering for protection and development of environment and constructions*. Associazione Geotecnica Italiana, Rome, Italy. CRC Press, pp 1228–1235
- Bird JF, Bommer JJ (2004) Earthquake losses due to ground failure. *Eng Geol* 75(2):147–179
- Boore DM, Stewart JP, Seyhan E, Atkinson GM (2014) NGA-West 2 equations for predicting PGA, PGV, and 5%-damped PSA for shallow crustal earthquakes. *Earthq Spectra* 30:1057–1085
- Bozzano F, Gambino P, Prestininzi A, Scarascia Mugnozza G, Valentini G (1998) Ground effects induced by the Umbria-Marche earthquakes of September–October 1997, Central Italy. In: Balkema AA (eds) *Proceedings of the 8th international congress of the international association for engineering geology and the environment*, Vancouver, Canada, 21–25 September, 1998, Rotterdam, The Netherlands, pp 825–830
- Campbell KW, Bozorgnia Y (2014) NGA-West2 ground motion model for the average horizontal components of PGA, PGV, and 5% damped linear acceleration response spectra. *Earthq Spectra* 30:1087–1115
- Carro M, De Amicis M, Luzi L, Marzorati S (2003) The application of predictive modeling techniques to landslides induced by earthquakes: the case study of the 26 September 1997 Umbria–Marche earthquake (Italy). *Eng Geol* 69:139–159
- CERI working group, Martino S, Caporossi P, Della Seta M, Esposito C, Fantini A, Fiorucci M, Iannucci R, Marmoni GM, Mazzanti P, Missoni C, Moretto S, Rivellino S, Romeo RW, Sarandrea P, Troiani F, Varone C (2016). *Sisma Centro Italia: Amatrice, Visso, Norcia Effetti-Interazione rete infrastrutturale*. Available at <http://www.ceri.uniroma1.it/>. Last Accessed 19 April 2018
- Chiaraluce L, Amato A, Cocco M, Chiarabba C, Selvaggi G, Di Bona M, Piccinini D, Deschamps A, Margheriti L, Courboux F, Ripepe M (2004) Complex normal faulting in the apennines thrust-and-fold belt: the 1997 seismic sequence in central Italy. *Bull Seismol Soc Am* 94:99–116
- Chiou BS-J, Youngs RR (2014) Update of the Chiou and Youngs NGA model for the average horizontal component of peak ground motion and response spectra. *Earthq Spectra* 30:1117–1153
- Choi J-K, Won J-S, Lee S, Kim S-W, Kim K-D, Jung H-S (2011) Integration of GIS and SAR interferometry for a coal mine subsidence hazard map in Taebaek, Korea. *Int J Remote Sens* 32:8161–8181
- Cotecchia V, Del Prete M (1984) The reactivation of large flows in the parts of Southern Italy affected by the earthquake of November 1980, with reference to the evolutive mechanism. *Proceedings of the fourth international symposium on landslides*, Toronto, Canada 2:33–37
- Cotecchia V, Guerricchio A, Melidoro G (1986) The Geomorphogenetic Crisis Triggered by the 1783 earthquake in Calabria (Southern Italy). *Proceedings of the international symposium on engineering geology problems in seismic areas*, Bari, Italy 6:245–304
- Cruden DM, Varnes DJ (1996) Landslide types and processes. In: Turner, Shuster (eds) *Landslides: investigation and mitigation*. Transportation Research Board, Special Reports 247:36–75
- D’Elia B, Esu F, Pellegrino A, Pescatore T (1985) Some effects on natural slope stability induced by the 1980 Italian earthquake. In: *Proceedings of the eleventh international society of soil mechanics and foundation engineering conference*, San Francisco, USA
- Esposito E, Porfido S, Simonelli AL, Mastrolorenzo G, Iaccarino G (2000) Landslides and other surface effects induced by the 1997 Umbria-Marche seismic sequence. *Eng Geol* 58:353–376
- Fielding EJ, Talebian M, Rosen PA, Nazari H, Jackson A, Ghorashi M, Walker R (2005) Surface ruptures and building damage of the 2003 Bam, Iran, earthquake mapped by satellite synthetic aperture radar interferometric correlation. *J Geophys Res* 110:B03302

- Franke KW, Lingwall BN, Zimmaro P, Kayen RE, Tommasi P, Chiabrando F, Santo A (2018) Phased reconnaissance approach to documenting landslides following the 2016 Central Italy earthquakes. *Earthq Spectra* 34:1693–1719
- Galadini F, Falcucci E, Gori S, Zimmaro P, Cheloni D, Stewart JP (2018) Active faulting in source region of 2016–2017 central Italy earthquake sequence. *Earthq Spectra* 34:1557–1583
- Galli P, Peronace E, Brammerini F, Castenetto S, Naso G, Cassone F, Pallone F (2016) The MCS intensity distribution of the devastating 24 August 2016 earthquake in central Italy (MW 6.2). *Ann Geophys* 59, FAST TRACK 5. <https://doi.org/10.4401/ag-7287>
- GEER (2017) Engineering reconnaissance following the October 2016 Central Italy earthquakes. In: Version 2, Zimmaro, Stewart (eds) GEER Association Report No. GEER-050D. <https://doi.org/10.18118/G6HS39>
- GEER (2016) Engineering reconnaissance of the 24 August 2016 Central Italy Earthquake. In: Version 2, Zimmaro, Stewart (eds). GEER Association Report No. GEER-050B. <https://doi.org/10.18118/G61S3Z>
- Gigli G, Morelli S, Fornera S, Casagli N (2014) Terrestrial laser scanner and geomechanical surveys for the rapid evaluation of rockfall susceptibility scenarios. *Landslides* 11:1–14
- Gori S, Falcucci E, Galadini F, Zimmaro P, Stewart JP, Kayen RE, Lingwall B, Moro M, Saroli M, Pizzi A, Di Domenica A (2018) Surface faulting caused by the 2016 Central Italy seismic sequence: field mapping and Lidar/UAV imaging. *Earthq Spectra* 34:1585–1610
- Hungr O, Leroueil S, Picarelli L (2014) The Varnes classification of landslide types, an update. *Landslides* 11:167–194
- INGV (2016) Gruppo di Lavoro INGV sul terremoto di Amatrice. Secondo rapporto di sintesi sul Terremoto di Amatrice MI 6.0 del 24 Agosto 2016 (Italia Centrale). <https://doi.org/10.5281/zenodo.154400>
- ISPRA (2016) Gruppo di Lavoro ISPRA. Report attività svolta da ISPRA in data 25–26/08/2016. Centro per la microzonazione sismica e le sue applicazioni. Available at: <https://www.isprambiente.gov.it/files2017/notizie/sisma/ReportsinteticoISPRAagosto16marzo17.pdf>. Last Accessed 18 Nov 2021
- Jayaram N, Baker JW (2009) Correlation model for spatially distributed ground-motion intensities. *Earthq Eng Struct Dynam* 38:1687–1708
- Jo M-J, Won J-S, Kim S-W, Jung H-S (2010) A time-series SAR observation of surface deformation at the southern end of the San Andreas fault zone. *Geosci J* 14:277–287
- Jung H-S, Lu Z, Won JS, Poland MP, Miklius A (2011) Mapping three-dimensional surface deformation by combining multiple-aperture interferometry and conventional interferometry: application to the June 2007 eruption of Kilauea volcano, Hawaii. *IEEE Geosci Remote Sens Lett* 8:34–38
- Keefer DK (1984) Landslides caused by earthquakes. *Geol Soc Am Bull* 95:406–421
- Keefer DK (1985) Landslides caused by earthquakes: reply. *Geol Soc Am Bull* 96:1093–1094
- Keefer DK (2002) Investigating landslides caused by earthquakes—a historical review. *Surv Geophys* 23:473–510
- Lanzo G, Tommasi P, Ausilio E, Aversa S, Bozzoni F, Cairo R, d’Onofrio A, Durante MG, Foti S, Giallini S, Mucciacciaro M, Pagliaroli A, Sica S, Silvestri F, Vessia G, Zimmaro P (2018) Reconnaissance of geotechnical aspects of the 2016 Central Italy earthquakes. *Bull Earthq Eng* 17:5495–5532
- Lee W, Lu Z, Won J-S, Jung H-S, Dzurisin D (2013) Dynamic deformation of Seguam Island, Alaska, 1992–2008, from multi-interferogram InSAR processing. *J Volcanol Geotherm Res* 260:43–51
- Pavlidis S, Chatzipetros A, Papathanasiou G, Georgiadis G, Sboras S, Valkaniotis S (2017) Ground deformation and fault modeling of the 2016 sequence (24 Aug–30 Oct) in central Apennines (Central Italy). *Bull Geol Soc Greece* 51:76–112
- Piatanesi A, Cirella A (2009) Rupture process of the 2009 Mw6.3 L’Aquila (Central Italy) earthquake from nonlinear inversion of strong motion and GPS data. Istituto Nazionale di Geofisica e Vulcanologia (INGV), Rome, Italy

- Polcari M, Montuori A, Bignami C, Moro M, Stramondo S, Tolomei C (2017) Using multi-band InSAR data for detecting local deformation phenomena induced by the 2016–2017 Central Italy seismic sequence. *Remote Sens Environ* 201:234–242
- Rathje EM, Carr LP (2010) Satellite observations of landslides caused by the 2008 Wenchuan earthquake in China. In: *Proceedings, 9th US national and 10th Canadian conference on earthquake engineering: reaching beyond borders*, July 2010, Toronto, Canada
- Rathje EM, Franke KW (2016) Remote sensing for geotechnical earthquake reconnaissance. *Soil Dyn Earthq Eng* 91:304–316
- Rodríguez CE, Bommer JJ, Chandler RJ (1999) Earthquake-induced landslides: 1980–1997. *Soil Dyn Earthq Eng* 18:325–346
- Romeo S, Di Matteo L, Melelli L, Cencetti C, Dragoni W, Fredduzzi A (2017) Seismic-induced rockfalls and landslide dam following the October 30, 2016 earthquake in Central Italy. *Landslides* 14:1457–1465
- Sarconi M (1784) *Osservazioni fatte nelle Calabrie e nella frontiera di Valdemone sui fenomeni del tramoto del 1783 e sulla geografia fisica di quelle regioni*. Reale Accademia delle Scienze e Belle Lettere. Naples, Italy
- Sextos A, De Risi R, Pagliaroli A, Foti S, Passeri F, Ausilio E, Cairo R, Capatti MC, Chiabrando F, Chiaradonna A, Dashti S, De Silva F, Dezi F, Durante MG, Giallini S, Lanzo G, Sica S, Simonelli AL, Zimmaro P (2018) Local site effects and incremental damage of buildings during the 2016 Central Italy earthquake sequence. *Earthq Spectra* 34:1639–1669
- Sieberg A (1930) *Geologie der Erdbeben*. Handbuch der Geophysic 2(4):552–554 [Tabb. 100, 101, 102, 103], Berlin, Germany
- Stewart JP, Lanzo G, Pagliaroli A, Scasserra G, Di Capua G, Peppoloni S, Darragh R, Gregor N (2012) Ground motion recordings from the Mw 6.3 2009 L'Aquila earthquake in Italy and their engineering implications. *Earthq Spectra* 28:317–345
- Yun S-H, Fielding EJ, Simons M, Rosen P, Owen S, Webb F (2011) Damage proxy map of M 6.3 Christchurch earthquake using InSAR coherence. *Fringe Workshop. Advances in the science and applications of SAR interferometry from ESA and 3rd party missions*. Frascati, Italy. Available at: [https://earth.esa.int/documents/10174/1567329/Yun\\_FRINGE2011.pdf](https://earth.esa.int/documents/10174/1567329/Yun_FRINGE2011.pdf)
- Yun S-H, Hudnut K, Owen S, Webb F, Simons M, Sacco P, Gurrola E, Manipon G, Liang C, Fielding EJ, Milillo P, Hua H, Coletta A (2015) Rapid damage mapping for the 2015 Mw 7.8 Gorkha earthquake using synthetic aperture radar data from COSMO–SkyMed and ALOS-2 satellites. *Seismol Res Lett* 86:1549–1556
- Zhang L, Lu Z, Ding X, Jung H-S, Feng G, Lee C-W (2012) Mapping ground surface deformation using temporarily coherent point SAR interferometry: application to Los Angeles Basin. *Remote Sens Environ* 117:429–439
- Zimmaro P, Scasserra G, Stewart JP, Kishida T, Tropeano G, Castiglia M, Pelekis P (2018) Strong ground motion characteristics from 2016 central Italy earthquake sequence. *Earthq Spectra* 34:1611–1637
- Zimmaro P, Stewart JP (2017) Site-specific seismic hazard analysis for Calabrian dam site using regionally customized seismic source and ground motion models. *Soil Dyn Earthq Eng* 94:179–192